Draft version October 30, 2013
Preprint typeset using LaTeX style emulateapj v. 02/09/03

TURBULENT AMBIPOLAR DIFFUSION: NUMERICAL STUDIES IN 2D

Fabian Heitsch[1,2], Ellen G. Zweibel[1,2,3], Adrianne D. Slyz[4], and Julien E.G. Devriendt[4]

Draft version October 30, 2013

ABSTRACT

Under ideal MHD conditions the magnetic field strength should be correlated with density in the interstellar medium (ISM). However, observations indicate that this correlation is weak. Ambipolar diffusion can decrease the flux-to-mass ratio in weakly ionized media; however, it is generally thought to be too slow to play a significant role in the ISM except in the densest molecular clouds. Turbulence is often invoked in astrophysical problems to increase transport rates above the (very slow) laminar values predicted by kinetic theory. We describe a series of numerical experiments addressing the problem of turbulent transport of magnetic fields in weakly ionized gases. We show, subject to various geometrical and physical restrictions, that turbulence in a weakly ionized medium rapidly diffuses the magnetic flux to mass ratio B/ρ through the buildup of appreciable ion-neutral drifts on small scales. These results are applicable to the fieldstrength - density correlation in the ISM, as well as the merging of flux systems such as protostar and accretion disk fields or protostellar jets with ambient matter, and the vertical transport of galactic magnetic fields.

Subject headings: diffusion — MHD — turbulence — methods:numerical — ISM:magnetic fields

1. INTRODUCTION

Two dimensionless parameters control the degree to which galactic magnetic fields are frozen to the interstellar gas. One, the magnetic Reynolds number R_M, is the ratio of the Ohmic diffusion time to the dynamical time, and is typically of order 10^{15} - 10^{21}. The second, the ambipolar Reynolds number R_{AD}, is the ratio of the ion-neutral drift time to the dynamical time. This number is typically many orders of magnitude less than R_M, and can approach unity in dense molecular gas. Based on these estimates, magnetic fields should be nearly perfectly frozen to the plasma component of the gas, and generally quite well frozen to the neutrals, except in the densest, nearly neutral regions.

Thus, the ratio of magnetic fieldstrength to gas density B/ρ is determined primarily by dynamical rather than by microscopic processes. Parameterizing the $B-\rho$ relation by $\kappa \equiv d\ln B/d\ln\rho$, one finds $\kappa = 1$ for compression perpendicular to $\mathbf{B}$, $\kappa = 2/3$ for isotropic compression, $\kappa \sim 1/2$ for self-gravitating, magnetically subcritical clouds, and $\kappa = 0$ for compression parallel to $\mathbf{B}$.

Observations of the $B-\rho$ relation in molecular gas indeed show that the strongest fields are associated with the densest gas (Crutcher (1999), Bourke et al. (2001), Sarma et al. (2002)). The correlation is consistent with $\kappa \sim 0.5$, although there is so much dispersion, particularly when upper limits are included, that this relation is perhaps only an upper envelope. In atomic gas, the $B-\rho$ relation is consistent with $\kappa \sim 0$ over three orders of magnitude in ρ (Troland & Heiles 1986). Observational effects alone can introduce substantial scatter because all measurements are averages along the line of sight and over the telescope beam width, ρ may not be accurately determined, and because only the line-of-sight component of $\mathbf{B}$ is measurable. However, even allowing for the possibility that the observational scatter is large, the $B-\rho$ relation is strikingly flat. Moreover, there is a mean density jump of at least a factor of 50 when going from atomic to molecular gas, whereas the corresponding mean magnetic field strength seems to increase by a factor of two or three at most.

At first sight, the simplest explanation of the observed $B-\rho$ relation is that dense regions in the ISM arise primarily from compression parallel to $\mathbf{B}$. Arguments against this as the sole explanation are quantitative rather than qualitative. In order to collimate the flow, the magnetic energy density should dominate the turbulent energy density, but the field is at or below equipartition. And, if giant molecular clouds are assembled by 1D compression, they must sweep up material over nearly a kpc, too large a scale on which to expect coherent flow (Mestel 1985).

In astrophysical environments, the microscopic diffusivities - whether viscous, resistive, or chemical - are often far too small to explain the transport that apparently takes place. However, diffusion rates can be enhanced by turbulence. Turbulence accelerates transport because it creates small scale structure, which diffuses faster than the original large scale structure and smoothes the large scale gradients. In a turbulent flow with characteristic velocity u and correlation time τ, the effective diffusivity λ_e is argued to be of order $u^2\tau$ (see eq. [A6]).

Therefore, in this paper, we investigate whether turbulence has a similar effect on the transport of magnetic fields with respect to the neutral gas. Because the interstellar magnetic field is subject to ion-neutral drift at scales much larger than the resistive scale, we ignore resistive effects, except to control numerical diffusion in our calculation, and concentrate on the properties of ion-neutral drift in a turbulent medium. Although our work is motivated by the $B-\rho$ relation observed in the interstellar medium, it is also relevant to other problems, including transport of magnetic fields in weakly ionized accretion disks and entrainment of molecular gas by pro-

[1] U Wisconsin-Madison, 475 N Charter St, Madison, WI 53706, U.S.A.
[2] JILA/U Colorado, Boulder, CO 80309-0440, U.S.A.
[3] Center for Magnetic Self-Organization in Laboratory & Astrophysical Plasmas
[4] U Oxford, Keble Road, OX1 3RH Oxford, UK

tostellar outflows.

In §2, we review the theoretical basis for turbulent ambipolar drift and summarize previous results. In §3 we introduce our model. Section 4 is a description of the numerical method and its validation. The main results are presented in §5. Finally, we mention other applications in the concluding section, together with a summary.

2. BACKGROUND

Consider a medium in which the ionization is sufficiently low that the neutral and total densities, ρ_n and ρ, are interchangeable, as are the neutral and center of mass velocities $\mathbf{u}_n$ and $\mathbf{u}$. Under these conditions, the continuity equation

$$\frac{\partial \rho}{\partial t} = -\nabla \cdot \rho \mathbf{u} \tag{1}$$

and magnetic induction equation

$$\frac{\partial \mathbf{B}}{\partial t} = \nabla \times (\mathbf{u}_i \times \mathbf{B}) \tag{2}$$

can be combined to yield an equation for $\mathbf{B}/\rho$

$$\left(\frac{\partial}{\partial t} + \mathbf{u}\cdot\nabla\right)\frac{\mathbf{B}}{\rho} = \frac{\mathbf{B}}{\rho}\cdot\nabla\mathbf{u} + \frac{1}{\rho}\nabla\times(\mathbf{u}_D\times\mathbf{B}), \tag{3}$$

where $\mathbf{u}_D \equiv \mathbf{u}_i - \mathbf{u}_n$ is the relative drift between the ions and the neutrals. The first term on the right hand side of equation (3) represents fieldline stretching, while the second term represents ambipolar diffusion.

In this paper, we restrict ourselves to a geometry in which all velocities are in the (x, y) plane, $\mathbf{B} = \hat{\mathbf{z}}B$, and all quantities are independent of z. Under these restrictions there is no fieldline stretching, and equation (3) reduces to

$$\left(\frac{\partial}{\partial t} + \mathbf{u}\cdot\nabla\right)\frac{B}{\rho} = -\frac{1}{\rho}\nabla\cdot(\mathbf{u}_D B). \tag{4}$$

If the timescales of interest are long compared to the ion-neutral collision time ν_{in}^{-1}, $\mathbf{u}_D$ is determined by balancing the Lorentz force on the ions against the frictional force on the neutrals (the so-called strong coupling approximation). For the geometry assumed here, the Lorentz force is due only to the magnetic pressure gradient, and

$$\mathbf{u}_D = -\frac{1}{\rho_i \nu_{in}}\nabla\frac{B^2}{8\pi}. \tag{5}$$

Substituting equation (5) into equation (4) yields

$$\left(\frac{\partial}{\partial t} + \mathbf{u}\cdot\nabla\right)\frac{B}{\rho} = \frac{1}{\rho}\nabla\cdot\lambda_{AD}\nabla B, \tag{6}$$

where

$$\lambda_{AD} \equiv \frac{B^2}{4\pi\rho_i\nu_{in}} \tag{7}$$

is the ambipolar diffusivity.

Equation (6) is almost, but not quite, an advection - diffusion equation for B/ρ. The difference is that the diffusive flux is proportional to ∇B, not $\nabla(B/\rho)$. As an immediate consequence, B/ρ will develop a large dispersion if ρ itself is advected by the turbulence as a passive scalar (see §5 5.5).

Equation (6) predicts a characteristic ambipolar diffusion time τ_{AD} for a field with characteristic lengthscale L_B

$$\tau_{AD} \equiv \frac{L_B^2}{\lambda_{AD}}, \tag{8}$$

We want to know for which turbulent flow speeds u and length scales L_e would such a field diffuse at a rate higher than the laminar rate. If the turbulence has a correlation time $\tau_c = L_e/u$, the turbulent diffusivity λ_e is of order $u^2\tau_c = L_e u$ (see eq. [A6]). The ratio of the ambipolar diffusion time τ_{AD} to the turbulent diffusion time τ_t is just the ratio of the two diffusivities: $\tau_{AD}/\tau_t = \lambda_e/\lambda_{AD}$. Therefore we are interested in the case $\lambda_e/\lambda_{AD} > 1$. This condition will be satisfied if the magnetic field is well frozen to the turbulent eddies. The degree of freezing is measured by the eddy ambipolar Reynolds number $R_{AD}(L_e, u)$, the ratio of the ambipolar diffusion time across the eddy, $\tau_{AD}(L_e)$ to the eddy correlation time. Assuming the eddy size L_e is related to u and τ_c by $L_e = u\tau_c$ we have

$$R_{AD}(L_e, u) \equiv \frac{\tau_{AD}(L_e)}{\tau_c} = \frac{L_e u}{\lambda_{AD}} = \left(\frac{u}{c_{Ai}}\right)^2 \tau_c \nu_{in}. \tag{9}$$

Inserting numerical values,

$$R_{AD}(L_e, u) = 9.4\times10^{-9}\, L_e\, u \left(\frac{n_n}{B}\right)^2 \frac{\mu_i\,\mu_n}{\mu_i+\mu_n}\, x_i, \tag{10}$$

where L_e is expressed in parsecs, u in km s^{-1}, B in Gauss, and n_n in cm^{-3}. The μ represent molecular weights, and x_i is the ionization fraction. The field is frozen to turbulent eddies which are larger than the size at which $R_{AD}(L_e, u) = 1$. For example, in gas with an ionization fraction 10^{-3}, $\mu_i/\mu_n \gg 1$, magnetic field $B = 5\mu G$, an internal velocity dispersion $u = 1$, and neutral density $n_n = 50$, this critical lengthscale is about 10^{-3}pc, corresponding to a column density of about 1.5×10^{17} cm^{-2}.

What diffusion rate is actually required to break the flux freezing and produce a flat $B-\rho$ relation? Suppose a coherent density structure of size L forms on a timescale τ, with an associated velocity U. The $B-\rho$ relation breaks down if the diffusion time is less than the formation time. In other words, if the relation

$$\lambda_{AD} < LU < \lambda_e \tag{11}$$

holds, then laminar ambipolar drift is too slow to break flux freezing but turbulence is fast enough.

If L, U, L_e, and u are related through the usual scaling laws for a turbulent cascade, then $U/u > 1$ whenever $L/L_e > 1$. Hence turbulent mixing can only destroy the $B-\rho$ relation in large scale structures which are controlled by additional physics, such as cooling or self gravity, or in regions with strong sources of small scale turbulence, such as velocity shear layers.

Equation (6) is the basis of three recent studies of the effects of turbulence on the rate of ambipolar drift. Zweibel (2002) demonstrated accelerated diffusion at approximately the eddy rate λ_e by finding exact solutions of equation (6) for random sequences of incompressible stagnation point flows, valid for a particular initial magnetic profile and initially constant density. Fatuzzo & Adams (2002) concentrated on the role of fluctuations in B, and hence λ_{AD}, in reducing τ_{AD}. They showed that fluctuations in fieldstrength lead to

a corresponding dispersion in ambipolar diffusion times. Kim & Diamond (2002) analyzed equation (6), assuming $\nabla \cdot \mathbf{u} \equiv 0$ and constant ρ, under the standard assumptions of quasilinear diffusion theory (QDT, see Appendix). They argued that the canonical turbulent diffusion rate $\lambda_e \sim u^2\tau$ is an upper limit which is approached for turbulence well frozen to the eddies.

Within the framework of QDT, the novel aspect of equation (6) is the right hand side, which consists of a nonlinear diffusion operator applied to B, not B/ρ. The latter distinction is unimportant as long as ρ is uniform. Kim & Diamond (2002) argue that diffusion reduces turbulent transport, because in a highly diffusive system, the field is not advected by the flow. While equation (3) shows that in the limit $\lambda_{AD} \equiv 0$ there is no diffusion in an absolute sense, we will see that the large scale component can decay by transferring power to the small scales.

Taken together, Zweibel (2002), Fatuzzo & Adams (2002), and Kim & Diamond (2002) support the proposition that ambipolar drift is accelerated in a turbulent medium, provided that the strong coupling approximation holds, and in the 2.5D geometry assumed in all three papers. The diffusion rate is enhanced by the development of small scale structure in the field, which increases the local drift velocity, and by the growth of fluctuations in fieldstrength, which increases the local diffusivity. When the former dominates, the diffusion rate is close to the canonical turbulent value $u^2\tau$, and nearly independent of the microscopic diffusivity.

Although these papers are suggestive, the picture they present is still incomplete. Due to the choice of initial condition, the difference between diffusion of B and diffusion of B/ρ is not addressed by any of the work, although the former describes transport of B from an Eulerian volume and the latter from a Lagrangian one. The respective roles of irreversible flux transport by ion-neutral drift and breakup of large scale structure into small scale fluctuations is not discussed by the QDT calculation, while the stagnation point calculation has yet to be embedded in a globally valid flow model. In the remainder of this paper, we report on a series of numerical experiments of the same basic problem which address some, but not all, of these limitations.

3. DESCRIPTION OF THE PROBLEM

3.1. *Assumptions and Equations*

As in §2, we consider the action of 2D flow (in the (x, y) plane) on a perpendicular magnetic field $\hat{\mathbf{z}}B$. Because we anticipate the formation of structure on small scales, we do not assume strong coupling (eq. [5]). Instead, we compute $\mathbf{u}_i$ by solving the ion equation of motion

$$\rho_i \left(\frac{\partial}{\partial t}\mathbf{u}_i + (\mathbf{u}_i \cdot \nabla)\mathbf{u}_i \right) = -\frac{1}{8\pi}\nabla B^2 - \rho_i \nu_{in}(\mathbf{u}_i - \mathbf{u}_n). \tag{12}$$

We assume that ρ_i is related to ρ_n through the condition of ionization equilibrium. Although this breaks down on short timescales, we have argued elsewhere that it is generally an excellent approximation (Heitsch & Zweibel 2003). We also neglect ion pressure relative to magnetic pressure. This is a good approximation in weakly ionized interstellar gas except near magnetic nulls, which are precluded by the choice of initial conditions (see §3 3.5).

We simplify the problem further by treating $\mathbf{u}_n$ as given. Although this so-called kinematic approach is frequently made in turbulent mixing problems, it is not particularly accurate in the interstellar medium, because the magnetic and turbulent pressures are comparable. However, in weakly ionized gas there is a lengthscale below which the neutrals and ions are not well coupled (see §3 3.2), and one can regard the dynamics as taking place below this critical scale. One consequence of treating the neutrals kinematically is that ρ itself behaves as a passive scalar. We could reach the same result by assuming zero temperature, and neglecting ion pressure.

With $\mathbf{u}_i$ determined from equation (12), we require only the magnetic induction equation to close the system. In the geometry considered here, the induction equation equation (2) is

$$\frac{\partial}{\partial t}B = -\nabla \cdot (\mathbf{u}_i B) + \lambda_\Omega \nabla^2 B, \tag{13}$$

where the second term on the RHS has the same form as Ohmic diffusion. We tune this last term so that it dominates the numerical diffusion.

3.2. *Linear Theory*

Equations (12) and (13) can be linearized to describe small perturbations about a uniform equilibrium state. The analytical solutions provide physical insight and are useful for numerical tests. Assuming the perturbations are Fourier modes which depend on (x, y, t) as $\exp[i(k_x x + k_y y - \omega t)]$ yields the dispersion relation

$$\omega = -\frac{\imath\nu_{in}}{2} \pm \sqrt{k^2\, c_{Ai}^2 - (\frac{\nu_{in}}{2})^2}, \tag{14}$$

where $k^2 \equiv k_x^2 + k_y^2$ and $c_{Ai} = B/\sqrt{4\pi\rho_i}$ is the Alfvén speed in the plasma.

If $kc_{Ai} \gg \nu_{in}/2$, the roots of equation (14) describe forward and backward propagating magnetosonic waves damped by ion-neutral friction

$$\omega \approx \pm kc_{Ai} - \imath\frac{\nu_{in}}{2}. \tag{15}$$

If $kc_{Ai} < \nu_{in}/2$, ω is purely imaginary. In the limit $kc_{Ai} \ll \nu_{in}/2$, the roots of equation (14) are given approximately by

$$\omega = -\imath\nu_{in} \tag{16}$$

$$\omega = -\imath\frac{k^2 c_{Ai}^2}{2\nu_{in}}. \tag{17}$$

Equations (15) and (16) can be compared to the dispersion relation which accounts for ion feedback on the neutrals (Kulsrud & Pearce 1969). According to this more complete treatment, ω is purely imaginary for $2\nu_{in}\sqrt{\rho_i/\rho} < kc_{Ai} < \nu_{in}/2$. The upper limit is exactly what is predicted by equation (14), and equation (15) agrees well with the exact dispersion relation. The lower limit is not predicted by equation (14). At k values well below this lower cutoff, the wave propagates at the bulk Alfvén speed $B/\sqrt{4\pi\rho}$. In this regime, the neutrals have time to be accelerated by the ions within one wave period. This does not happen in our model because we omit the drag force on the neutrals.

The solid line in Figure 1 shows the predicted dependence of the damping rate (i.e. the imaginary part of the wave frequency ω of eq. [14]) on ν_{in}. The damping mode changes at $2c_{Ai}k$ as expected. A discussion of the overplotted numerical results is left to §4 4.1.

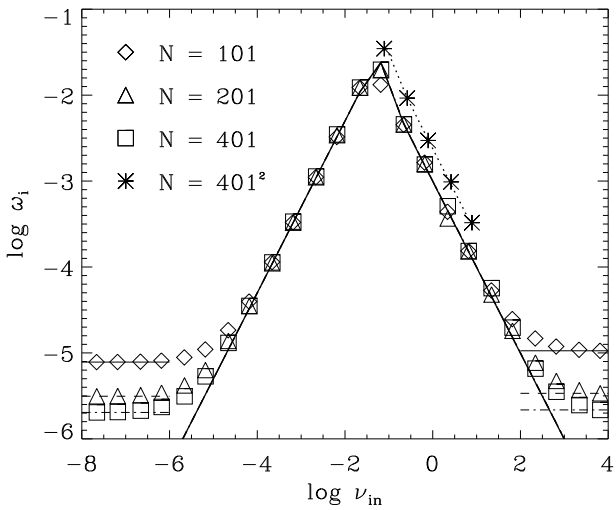

FIG. 1.— Decay rate ω_i against collision frequency ν_{in}, according to equation (14) for the 1D case (solid line) and the 2D case (dashed line). The symbols denote numerical results at resolutions as labeled in the plot. Note that the 2D case is shifted by exactly a factor of 2 with respect to the 1D result. The flat parts at low and high ν_{in} are caused by numerical diffusion, leaving roughly two orders of magnitude in ν_{in} in the declining branch of ω_i (eq. [17]) for numerical studies.

3.3. *The Neutral Flow*

We adopt a two-dimensional version of the divergence free, "circularly polarized" flow of Galloway & Proctor (1992), (hereafter GP-flow), which we write in component form as

$$u_{n,x} = \sqrt{\frac{3}{2}} v_f \cos(2\pi(k_f y + \epsilon \sin(2\pi k_f v_f t)))$$
$$u_{n,y} = \sqrt{\frac{3}{2}} v_f \sin(2\pi(k_f x + \epsilon \cos(2\pi k_f v_f t))). \quad (18)$$

We have chosen this flow because it has stretching properties (Galloway & Proctor (1992) show it to be a dynamo flow) and can be written in closed form. Its degree of chaos can be tuned through the choice of the parameter ϵ.[5] For $\epsilon = 0$ the flow is steady and possesses cellular structure at a single spatial scale. The corners of the cells are hyperbolic stagnation points near which the fluid undergoes exponential expansion along one axis and exponential compression along the other. Fluid circulates steadily around the center of its cell with an eddy turnover time of order

$$\tau_f = (k_f v_f)^{-1}. \quad (19)$$

Since each eddy retains its amount of fluid, we expect turbulent transport to be minimal.

The flow pattern for $\epsilon > 0$ can be visualized as eddies at a single scale travelling in snake-like patterns across the domain. The position of each eddy oscillates by ϵ/k_f. For $\epsilon \ll 1$, this is also roughly the size of the chaotic region. Advected quantities are not bound to the eddies, but travel from one to another, leading to turbulent transport.

[5] Note that ϵ contains a factor of 2π in our definition (eq. 18), thus being by that factor larger than the definition in Galloway & Proctor (1992).

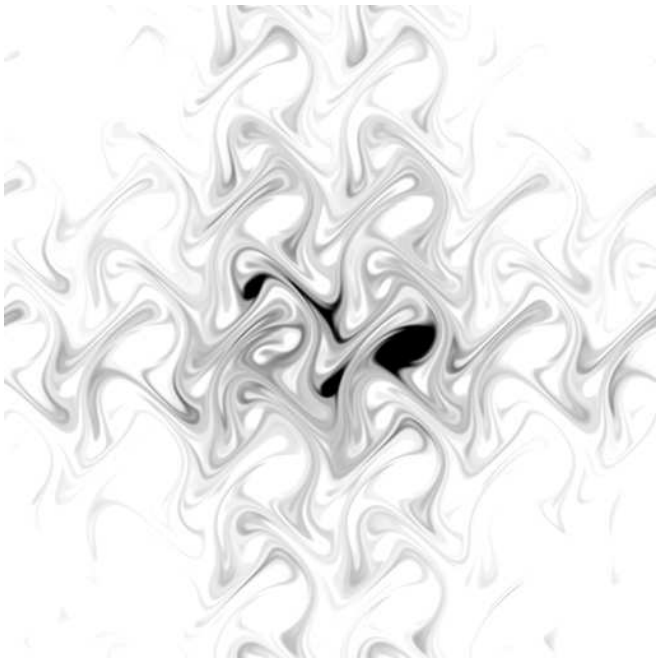

FIG. 2.— Tracer pattern caused by GP-flow after $t = 2\tau_f$. At $t = 0$, a tracer quantity is deployed into a circular region with diameter $L/4$. The GP cell number $\kappa_f = 5$, and $\epsilon = 0.3$. Resolution $N = 1601^2$.

Figure 2 shows an example of the GP-flow for κ_f, the number of cells per domain length L, equal to 5 and $\epsilon = 0.3$. At $t = 0$, we deploy a tracer quantity into a circular region with diameter $L/4$. The resulting tracer distribution is shown at $t = 2\tau_f$. We discuss the choice of ϵ in §5 5.1.

3.4. *Parameter Regimes*

There are four diffusivities: the numerical diffusivity λ_{num}, the magnetic diffusivity λ_Ω defined in equation (13), the ambipolar diffusivity λ_{AD} defined in equation (7), and the eddy diffusivity of the GP flow λ_e, which is $\mathcal{O}(v_f/k_f)$ (see eq. [A6]). Normalizing by λ_e and using equation (7), we require

$$\frac{\lambda_{num}}{\lambda_e} \ll \frac{\lambda_\Omega}{\lambda_e} \ll \frac{k_f c_{Ai}}{\nu_{in}} \frac{c_{Ai}}{v_f} \ll 1. \quad (20)$$

If equation (20) is fulfilled then numerical diffusion is smaller than all other diffusion, Ohmic diffusion is weaker than ambipolar diffusion, as it is in the interstellar medium, and eddy diffusion is faster than ambipolar diffusion, which allows us to test the hypothesis that turbulence enhances the rate of magnetic field redistribution. The last inequality is equivalent to requiring that the field is frozen to the eddies: $R_{AD} \gg 1$ (see eq. [9]).

We also seek a separation of lengthscales in the problem. The largest scale possible in a periodic domain is L, while the eddy scale is L/κ_f. The distinction between large and small scales can be maintained only if

$$\kappa_f \gg 1. \quad (21)$$

Finally, as we saw in equation (14), waves propagate only for sufficiently large wavenumbers. We are actually interested in the nonpropagation regime, because only in

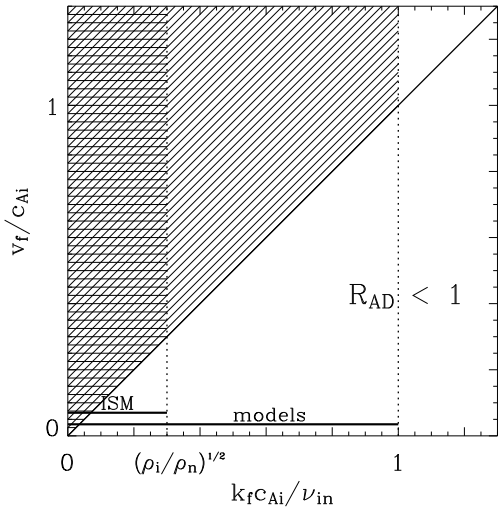

FIG. 3.— Valid regimes (schematically) for the ISM (horizontal lines) and the models (diagonal lines) under the strong coupling condition (eq. [5]). Vertical lines denote the nonpropagation limit according to equation (22) for the ISM and the models.

that case is the neutral flow imprinted on the ions. Thus, we require

$$\frac{k_f c_{Ai}}{\nu_{in}} \ll \frac{1}{2}. \tag{22}$$

When equation (22) is combined with the last condition in equation (20), the result is an upper limit on c_{Ai}/v_f. In the interstellar medium, where the magnetic field is close to equipartition with the turbulence, this quantity can be of order $(\rho/\rho_i)^{1/2}$, and hence quite large. For computational reasons, we are unable to make $k_f v_f/\nu_{in}$ as small as it should be, and therefore c_{Ai}/v_f will be smaller than it ought to be. However, there is no physical reason why turbulence cannot obey the proper ordering.

The restrictions on v_f/c_{Ai} and $k_f\, c_{Ai}/\nu_{in}$ resulting from equations (20) and (22) are sketched in Figure 3. For $k_f\, c_{Ai}/\nu_{in} > 1$, we are in the weakly damped branch, and anything below the diagonal thick line corresponds to $R_{AD} < 1$.

Taking these constraints together, the range of permissible ν_{in} is limited to at most 2 orders of magnitude, the range of B by slightly more than one order of magnitude, and κ_f between 5 and 10.

Tables 1 and 2, summarize the parameters for all models. For each combination of B and ν_{in}, we ran models for three GP forcing scales, namely $\kappa_f \in \{5, 7, 10\}$ at a resolution of $N = 801^2$. These models were completed by a set of pure tracer models (i.e. models with $\nu_{in} = 0$, and B subjected to turbulent diffusion only). To assess resolution effects on the results, we repeated the calculations at $N = 1601^2$.

3.5. *Initial Conditions*

We prepare our system with the initial conditions as given in equation (23) for the 2D case.

TABLE 1. AMBIPOLAR REYNOLDS NUMBER R_{AD}

$\downarrow B$ $\nu_{in} \rightarrow$	0.7	2.3	7.1	23.0
0.1	3.4×10^3	1.1×10^4	3.4×10^4	1.1×10^5
0.5	1.3×10^2	4.5×10^2	1.3×10^3	4.5×10^3
1.0	3.4×10^1	1.1×10^2	3.4×10^2	1.1×10^3
2.0	8.6×10^0	2.8×10^1	8.6×10^1	2.8×10^2

TABLE 2. RATIO $\lambda_{AD}/\lambda_\Omega$

$\downarrow B$ $\nu_{in} \rightarrow$	0.7	2.3	7.1	23.0
0.1	4.8×10^{-1}	1.4×10^{-1}	4.8×10^{-2}	1.4×10^{-2}
0.5	1.2×10^1	3.6×10^0	1.2×10^0	4.0×10^{-1}
1.0	4.8×10^1	1.4×10^1	4.8×10^0	1.4×10^0
2.0	1.9×10^2	5.8×10^1	1.9×10^1	5.8×10^0

$$B(x, y, 0) = B_0 + \frac{1}{2} B_1 \left[1 + \cos(k_P x) \cos(k_P y)\right]$$
$$\rho(x, y, 0) = \rho_0 - \frac{1}{2} \rho_1 \left[1 + \cos(k_P x) \cos(k_P y)\right]. \tag{23}$$

The 1D case is initialized similarly, with $y \equiv 0$. We add the offset in B to prevent field reversals, as these are known to lead to singularities in the presence of ambipolar drift (Brandenburg & Zweibel 1995; Mac Low & Smith 1997). We choose the perturbation amplitudes to be $B_1 = 0.1 B_0$, $\rho_1 = 0.1 \rho_0$, and the perturbation wave number k_P to be $2\pi/L$, i.e. the perturbations reside on the largest possible mode. According to the formalism of QDT discussed in the Appendix, the k_P components of B and ρ represent the large scale fields which are predicted to diffuse under the action of the small scale fields.

Ionization equilibrium (§3 3.1) implies that ρ_i is slaved to ρ. In the physical environments of interest here, $\rho_i \propto \rho^{1/2}$. Thus, the 10% perturbation of ρ imposed here (eq. [23]) would cause a 5% perturbation of ρ_i. For the sake of simplicity in the numerical scheme, we kept ρ_i constant in time and space. We believe the 5% variation in ion density to be too small to affect our results qualitatively.

To summarize, we initialize B and ρ using equations (23) and evolve the system in space and time using equations (12) and (13), where $\mathbf{u}_n$ in equation (12) is given by equation (18).

4. NUMERICS

4.1. *The scheme*

We solve equations (12) and (13) using a modified version of the 1st order gas-kinetic flux-splitting method described by Xu (1999) and Tang & Xu (2000). MUSCL[6] limiters allow a 2nd order reconstruction of the flow variables at the cell walls. As we are evolving only $\hat{\mathbf{z}} B(x, y, t)$, $\nabla \cdot \mathbf{B} \equiv 0$ is satisfied. The (otherwise passive) z velocity component serves as a tracer in order to measure the transport properties of the flow. The AD

[6] Monotone Upwind Schemes for Scalar Conservation Laws

drag force terms are added as external source terms to the cell-centered momenta and can be treated implicitly if necessary (similarly to Mac Low & Smith (1997); Tóth (1995)). The CFL-condition includes the diffusion timestep. As we are interested in representing the peak value of the initial magnetic field exactly, we employ a grid with an odd number of cells (the symmetry axis of the initial magnetic field goes through a cell center).

Figure 1 serves as a validation of the method for our problem. The decay of the magnetic field is measured in terms of the peak magnetic field amplitude against time. The initial conditions for 1D and 2D are given in equations (23). Apart from the fact that the numerical data points agree with the predictions in most cases at the 2%-level, we note the flattening at low and high ν_{in}. Both are caused by numerical diffusion. For small ν_{in}, this diffusion arises from the limited grid resolution. At ν_{num}, the point where the numerical results start to leave the predicted curve, the physical diffusion becomes smaller than the intrinsic numerical diffusion, which from then on governs the diffusive behavior. As soon as the numerical curve flattens, the results are meaningless for any physical problem. The timestep in this weakly damped branch is controlled by the diffusion timestep as in e.g. Mac Low et al. (1995).

For large ν_{in}, the diffusion is caused by the finite timesteps. If the collision time ν_{in}^{-1} becomes smaller than the timestep Δt, the number of collisions per Δt is limited. In other words, $\Delta t \ll \nu_{in}^{-1}$ must be guaranteed in order to prevent losing collisions and thus introducing numerical diffusion. The timesteps would be impractically small, and pursuing the computations would require an implicit treatment of the whole ion momentum equation. Although this is theoretically possible, we chose to implement a 2nd order Runge-Kutta time stepping method which guarantees results unaffected by numerical diffusion up to $\nu_{in} \approx 70$ (see Fig. 1).

Note that the predictions for the 2D decay rate (dashed line) coincides exactly with the numerical datapoints as well. It is this agreement which makes us confident in using the method for the investigation reported here. Further validation is presented in §5.

4.2. *Control of numerical diffusion*

As we mentioned in connection with equation (13), we control the diffusive behavior of the scheme at grid scale by introducing an artificial resistivity λ_Ω which dissipates the field above the grid scale. As is usually the case in astrophysical computations, λ_Ω is much larger than the physical resistivity. However, it is necessary because the GP-flow mixes scales very efficiently, leading to diffusion at the smallest possible scale after approximately an eddy-turnover time τ_f. This artificial resistivity guarantees well-behaved diffusion properties above the grid scale. It acts both on the magnetic field and the tracer field, which we identify as ρ. Thus, B and ρ are guaranteed to be smoothed on the smallest scales in the same manner.

In the flux-splitting scheme as described above, the amount of diffusion (last term of eq. [13]) is given by the slope of B, which in turn is computed during the reconstruction of the magnetic field at the cell walls. Thus we can implement the resistivity efficiently in our scheme. Restricting ourselves for the moment to a purely resistive

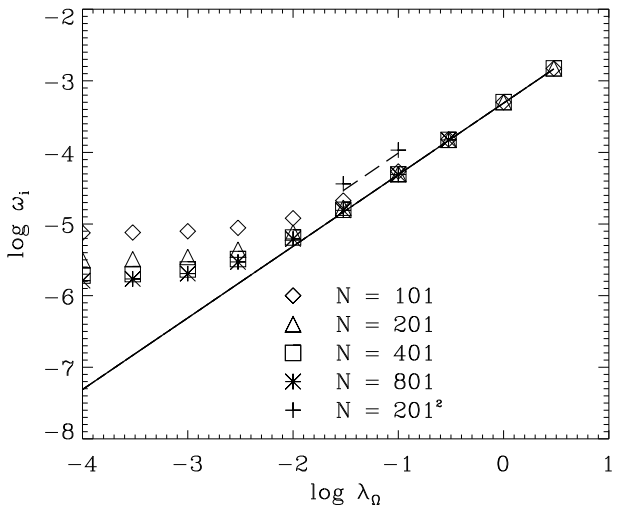

FIG. 4.— Decay rate ω_i against Ohmic diffusivity λ_Ω according to equation (24) (solid line) for the 1D case and (dashed line) for the 2D case. The symbols denote numerical results at resolutions as labeled in the plot. Note that the 2D case is exactly a factor of 2 shifted against the 1D result. The flat parts at low λ_Ω are caused by numerical diffusion.

medium – excluding ambipolar diffusion – the dispersion relation in the physically interesting regime (small λ_Ω) is given in 1D by

$$\omega = -\frac{\imath\lambda_\Omega k^2}{2} \pm \sqrt{c_{Ai}^2 k^2 - (\frac{\lambda_\Omega k^2}{2})^2}, \qquad (24)$$

where we are interested in the case $\lambda_\Omega k^2 \ll c_{Ai}^2 k^2$. The corresponding tests are shown in Figure 4. Numerical diffusion (flat part for small λ_Ω) occurs at the same level as for the implementation of ambipolar diffusion (see Fig. 1). Comparing the values of ω_i in Figure 4 with those of Figure 1 shows that our parameter space is limited by resistive diffusion.

5. RESULTS

We computed the evolution of B and of a tracer field for a set of realizations of the basic model described in §3; see Tables 1 and 2. We found that some, but not all, aspects of the transport of these quantities can be cast in terms of turbulent diffusion. After explaining how we measure the total diffusivity D in our models (see Appendix), we discuss the transport properties of the GP-flow in §5 5.1. In §5 5.2 and §5 5.3 we describe the evolution of the tracer ρ and the transport of B, respectively. Turbulent transport affects ρ and B in different ways, requiring a closer view on the ion flow (5 5.4). Finally in §5 5.5 we discuss the evolution of the flux to mass ratio B/ρ.

5.1. *Transport Properties of the GP-flow*

The transport properties of a flow are closely related to its Lyapunov exponents (see for example Drazin (1992)). We used a method implemented by Brumell, Cattaneo & Tobias (2001), based on Soward (1994) to calculate the Lyapunov exponents for the GP-flow. It follows the time evolution of the separation d of two points, initially an infinitesimal distance d_0 apart. If one or both points are located in a chaotic region, the separation grows exponentially. The grid resolution (in

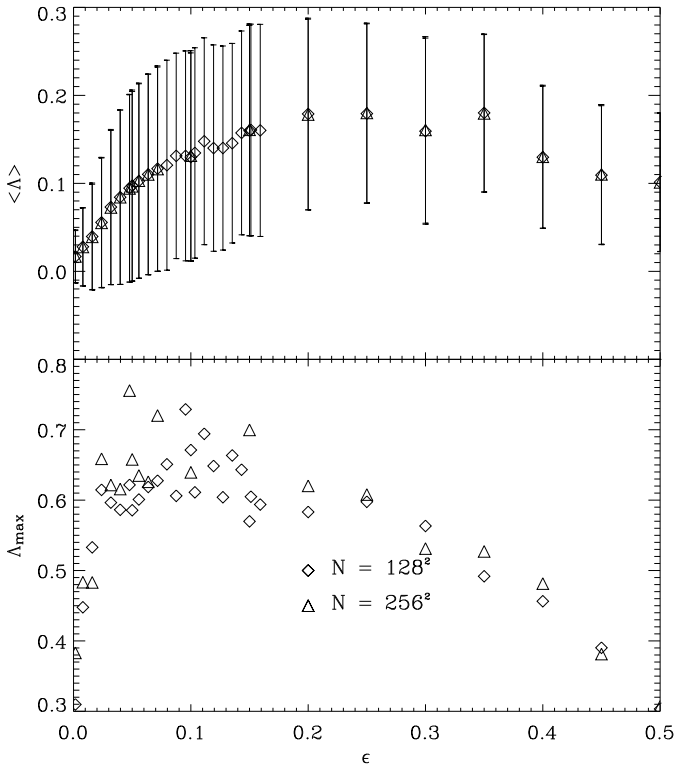

FIG. 5.— Mean and maximum Lyapunov exponents against ϵ. Error bars show the standard deviation across one frame. The maximum exponent Λ_{max} peaks at small ϵ because in this case, particle orbits are long and the chaotic regions are located at the cell boundaries. The flow's transport properties are determined primarily by the mean exponent $\langle\Lambda\rangle$.

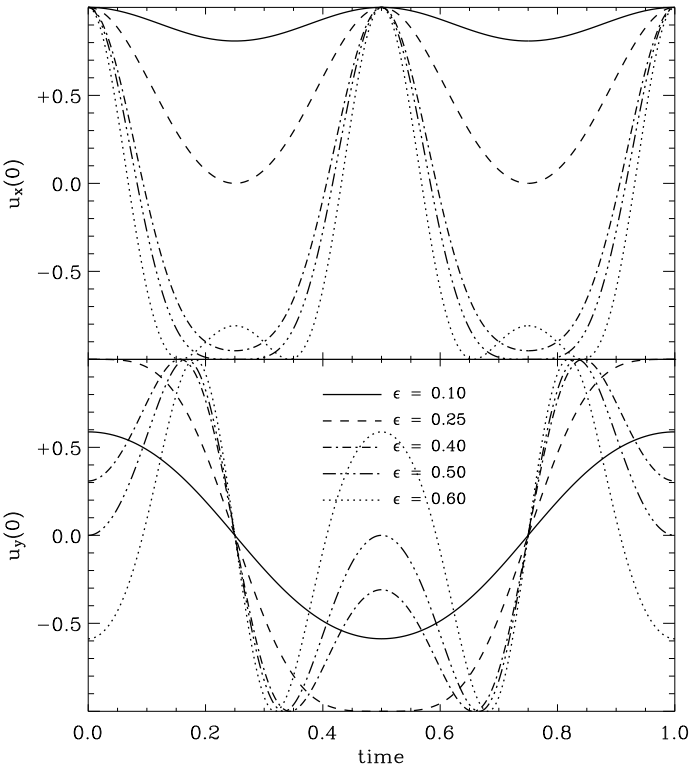

FIG. 6.— Velocities u_x and u_y according to equation (18) at $x = y = 0$. For $\epsilon > 0.25$ (maximum phase shift $\pi/2$), oscillations in u_y change to the next higher octave, the same happens for u_x for $\epsilon > 0.5$. By this, the coherent flow structure is disrupted.

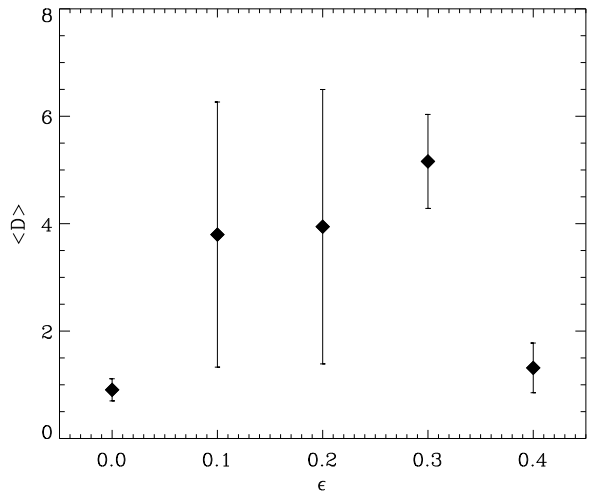

FIG. 7.— Diffusion constant D against complexity parameter ϵ (eq. [18]). The error bars give the standard deviations about the mean in equation (A9).

this case 128^2 and 256^2) is given by the number of paired starting points for following the particle trajectories, in our case distributed evenly over the flow domain.

Figure 5 gives the dependence of the domain averaged Lyapunov exponent $\langle\Lambda\rangle$ and maximum Lyapunov exponent Λ_{max} on ϵ. The mean Lyapunov exponent $\langle\Lambda\rangle$ peaks near $\epsilon \approx 0.25$, corresponding to a maximum phase shift of $\pi/2$ (see eq. [18]). The maximum exponent shows considerable scatter (mirrored in the large dispersions about the mean), but it too drops nearly monontonically for $\epsilon \gtrsim 0.25$. This came somewhat as a surprise to us, as a rising ϵ increases the time-dependence of the GP-flow.

Figure 6 explains this behavior. For $\epsilon > 0.25$ (maximum phase shift $\pi/2$), the frequency in velocity perturbations is doubled, disrupting the coherent flow structures and reducing the distance a test particle can be transported. Based on this qualitative argument, we expect a maximum in the transport rate for $\epsilon \simeq 0.25$.

Figure 7 demonstrates the connection between the complexity parameter ϵ in the GP-flow (eq. [18]) and the diffusion constant D (eq. [A9]). The diffusion constant peaks approximately at the ϵ for which the mean Lyapunov exponent $\langle\Lambda\rangle$ is maximal (see Fig. 5). The error bars reflect temporal fluctuations in D. Because we wish to maximize the transport, we chose $\epsilon = 0.3$ in all the models discussed subsequently.

We assessed the effect of the GP-flow's temporal periodicity on the transport rate by running some numerical experiments in which we replaced the factors of $k_f v_f t$ in equations (18) by random phases chosen from a uniform distribution in $(0, 2\pi)$ at fixed intervals in time. The resulting transport was less than for the GP flow with the same value of ϵ, so we pursued this model no further.

5.2. *Transport of a Tracer*

The transport of a passive scalar by the GP flow establishes a baseline against which the transport of the

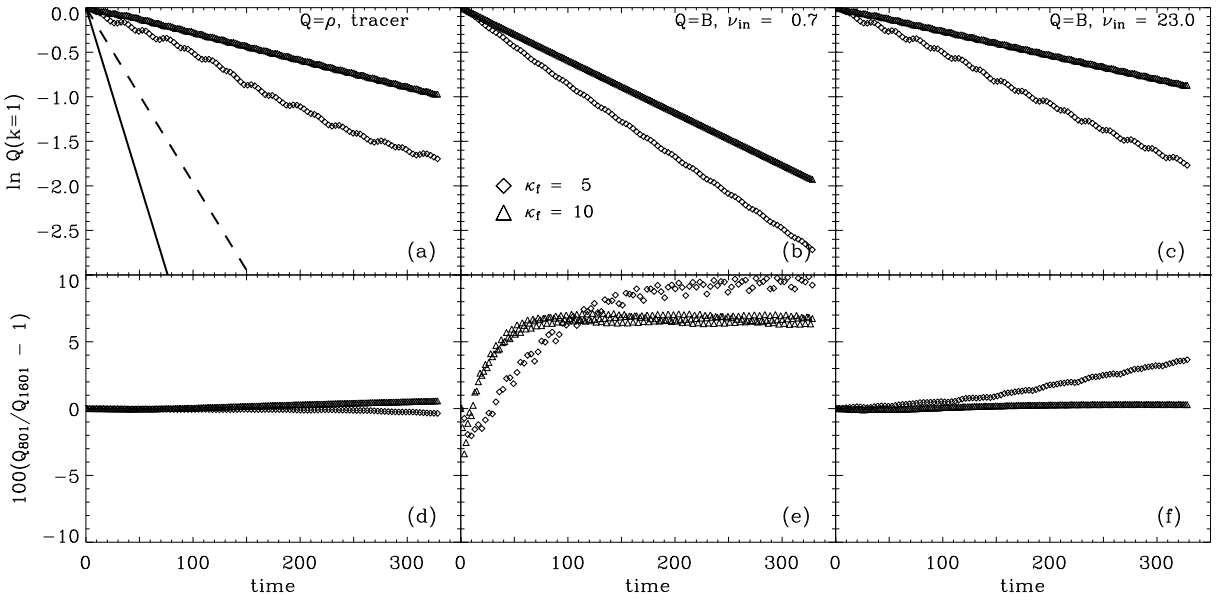

FIG. 8.— $(k = 1)$-mode of Q – where Q is either the density ρ or the magnetic field strength B – against time for resolution $N = 801^2$, $\kappa_f \in \{5, 10\}$ and $\epsilon = 0.3$. (a) Decay of density field. The solid ($\kappa_f = 5$) and dashed ($\kappa_f = 10$) lines stand for the turbulent decay rate expected from QDT (eq. [A6]). (b) Decay of magnetic field with $\nu_{in} = 0.7$. (c) Decay of magnetic field with $\nu_{in} = 23.0$. The slope gives the decay rate ω_i. Panels (d) to (f) show the difference $(Q_{801} - Q_{1601})/Q_{1601}$ in percent for runs of resolutions $N = 801^2$ and $N = 1601^2$ and parameters corresponding to panels (a) through (c). For $\nu_{in} = 0.7$, B develops strong peaks, which tend to be underresolved at $N = 801^2$.

magnetic field can be compared. It is also the relevant transport equation for the gas density ρ. We compute the transport by integrating equation (13) with $\mathbf{u}_i \equiv \mathbf{u}_{GP}$. The initial conditions are given by equations (23). Numerical diffusion is controlled as discussed in §4 4.2

Panel (a) of Figure 8 shows the time evolution of the average of the Fourier coefficients of $\rho_{k=1}$ (as defined following eq. [A8]) for two GP cell sizes ($\kappa_f = 5, 10$). The curves clearly demonstrate exponential decay. The difference in decay rates between the $\kappa_f = 5$ and $\kappa_f = 10$ cases agrees reasonably well with the expected $u^2\tau$ scaling of the turbulent diffusivity, since doubling κ_f decreases τ by a factor of 2 (eq. [19]). We note that the decay rates do not reach the values predicted by QDT (eq. [A6])[7]. The bumps in the curves are caused by time variations in the GP flow. Not only does the temporal frequency of the bumps correspond to the GP frequency, but the difference between two spatial resolutions (Fig. 8(d)) is very small over the duration of the calculation.

Figure 9 gives D as defined in equation (A9) for the same GP tracer models as in Figure 8. The settling effect of larger GP cell numbers is clearly visible. Note again that the different resolutions give identical results.

The top row of panels in Figure 10 show Fourier spectra of ρ for $\kappa_f \in \{5, 7, 10\}$. The vertical dashed lines indicate multiples of κ_f. All spectra display at least two branches with significantly different power. The values in the maximum branch group at $n\kappa_f \pm 1$, with $n \in \{1, 2, ...\}$. This is a direct consequence of the nature of the advection operator. The velocity $\mathbf{u}$ with its single scale κ_f initially beats together with the density perturbation, which is

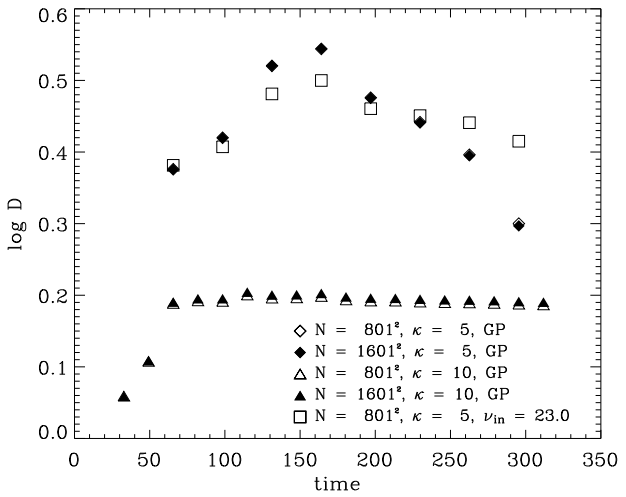

FIG. 9.— Diffusion constant (eq. [A9]) for the turbulent decay of the passive scalar, identified with the density ρ. The open squares denote results for turbulent ambipolar diffusion at the highest collision frequency ($\nu_{in} = 23.0$), demonstrating that for large collision frequencies the ions follow the GP-flow closely.

at $k = 1$ (see eq. [23]). This creates density structure at $\kappa_f \pm 1$. Advection of this secondary structure generates power at $2\kappa_f \pm 1$, and so on. The spectra should have power at these wavenumbers only; the power seen in Figure 10 at other k (all branches except the maximum branch) is entirely due to numerical noise[8]. The amplitude of the noise is 2-3 orders of magnitude less than the power at wavenumbers $n\kappa_f \pm 1$ (the maximum branch) up to the Nyquist k, which we regard as acceptable.

[7] This does not come as a surprise since QDT provides an estimate whose general assumptions are quite different from the assumptions made here: e.g, the GP-flow has a single scale and it is spatially and temporally periodic. The oscillation of the eddies in position prevents the maximum stretching of fluid elements in GP-cell corners.

[8] Although eqs. (12) and (13) are solved in double precision, the Fourier transform is computed in single precision.

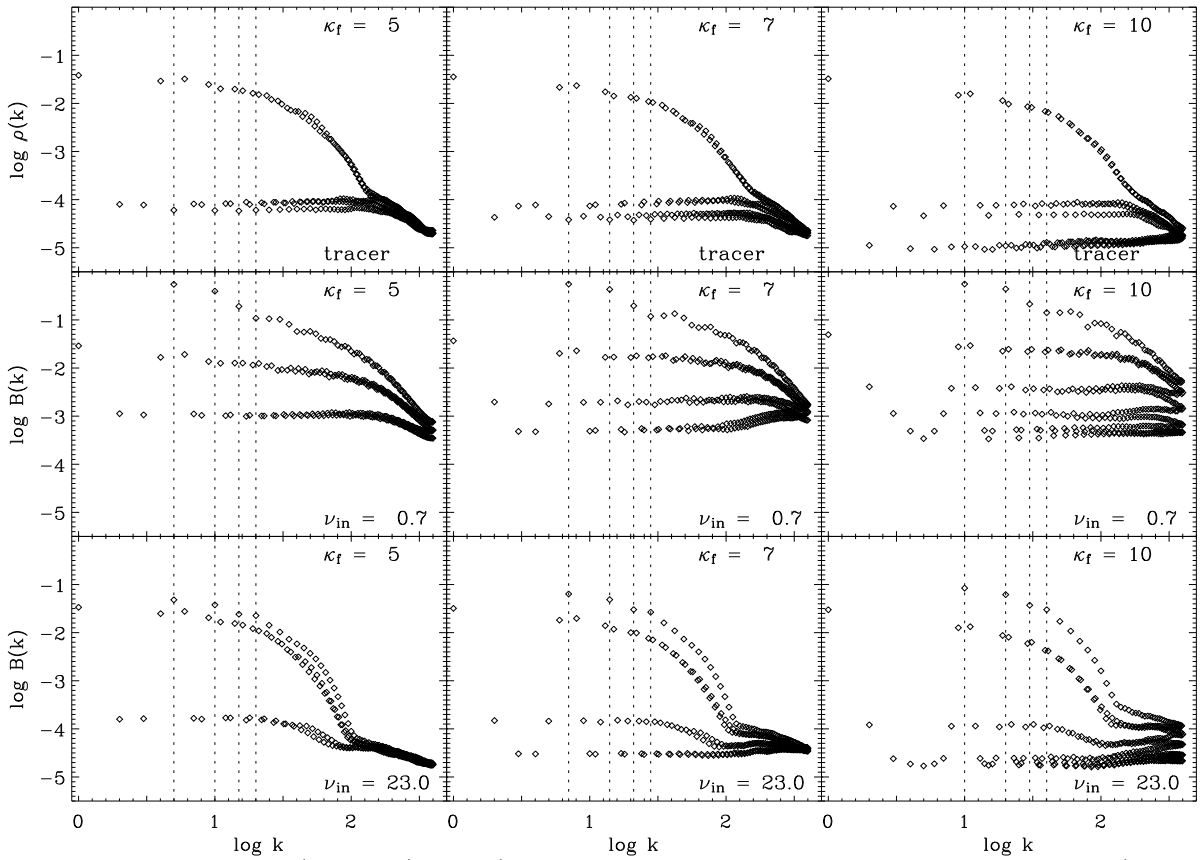

FIG. 10.— Fourier spectra of ρ (upper row) and B (lower rows for minimum and maximum collision frequency ν_{in}) for $\kappa_f \in \{5, 7, 10\}$. Vertical dashed lines denote multiples of κ_f (see text). Resolution $N = 801^2$. Each of the nine plots contains one spectrum. The Nyquist $k_N = 400$.

5.3. *Transport of the magnetic field*

Panels (b) and (c) of Figure 8 show the decay of the $(\pm 1, \pm 1)$ Fourier coefficients of B for two resolutions and two collision frequencies. The decay rates, when averaged over the GP flow period, are well fit by exponentials, and the scaling of the rates with κ_f is consistent with turbulent diffusion. The decay rate at the higher collision frequency is close to the GP rate shown in the leftmost panel. At the lower collision frequency, the field decays substantially faster because of the relatively large value of λ_{AD} in that case: the turbulent and laminar diffusivities are additive. The difference between these cases reflects the greater degree to which the ion flow is slaved to the neutral flow in the high collision frequency case.

Panels (e) and (f) of Figure 8 give the differences between these calculations for two resolutions. At the higher collision frequency, the differences increase gradually with time and remain small over the duration of the calculation (although they are larger than the corresponding differences for the tracer ρ shown in the lower left panel). At the low collision frequency, the difference grows quickly and saturates at about 10%. This shows the increased role of small scale structure in $\mathbf{u}_i$ at low collision frequencies. Smaller ν_{in} lead to larger compression and thus stronger peaks in B, which in turn tend to be underresolved at $N = 801^2$.

The diffusivities D computed according to equation (A9) for the two resolutions are nearly indistinguishable (Fig. 11). The good agreement between the theoretically predicted quiescent diffusion rates λ_{AD} and the numerical result validates our method of measuring D as well as provides an additional test of the underlying numerics. The approximate invariance of D over time, and insensitivity of D to ν_{in}, show that the transport of B is well described as turbulent diffusion (the small offset between the turbulent diffusivity for $\nu_{in} = 0.7$ and the other cases is again caused by the relatively large value of λ_{AD} in that case).

Because the ion flow is modified by Lorentz forces, we investigated the dependence of D on magnetic field-strength. Figure 12 plots the time-averaged D – denoted $\langle D \rangle$ – for four collision strengths and four magnetic field strengths. The laminar diffusivities (lines) follow the expected dependence of diffusivity on B. In contrast, the turbulent diffusivities (calculated by measuring D in a turbulent model and subtracting λ_{AD}) depend only marginally on B, despite the fact that the Alfvén Mach number varies from less than a tenth to slightly greater than unity. Note that at the lowest value of B, the quiescent diffusion rates are nearly independent of ν_{in}: at this value of B, the quiescent diffusivities are completely controlled by λ_Ω. On the other hand, at the highest value of B and lowest value of ν_{in}, the laminar diffusivity dominates the turbulent one. This case is less interesting to us for studies of the ISM.

The Fourier spectra of B are shown in the second and

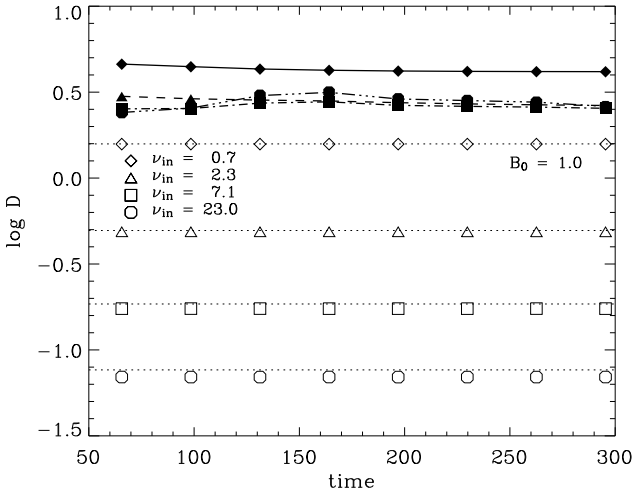

FIG. 11.— Diffusivities D against time according to equation (A9), for quiescent decay (open symbols) and turbulent decay (filled symbols for $N = 801^2$, thick lines for $N = 1601^2$). The quiescent diffusivities correspond to the theoretical predictions (dotted lines), and the turbulent diffusivities are nearly constant for the larger ν_{in}.

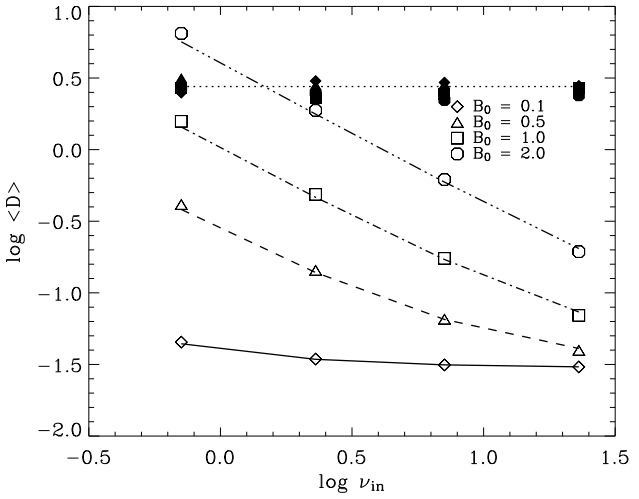

FIG. 12.— Diffusivities D as in Figure 11, but averaged over time, and for various field strengths. Open symbols give again quiescent rates and filled symbols stand for turbulent rates with the quiescent rates subtracted (see text). Note that the modelled quiescent rates reproduce the analytical predictions from $\lambda_{AD} + \lambda_\Omega$ (thick lines). The horizontal dotted line gives the turbulent diffusion rate for ρ, i.e. the pure GP-transport diffusion.

third rows of Figure 10 for two collision frequencies and $\kappa_f \in \{5, 7, 10\}$. In striking contrast to the spectra of ρ (top row of this figure), the spectra peak at multiples of κ_f. This effect is particularly strong at the low collision frequency, and provides graphical evidence that the transport of B to small scales is quite different from that of ρ. The disparity must be caused by differences between $\mathbf{u}_i$ and the GP flow, i.e. the ion-neutral drift. To see this, we rewrite the induction equation (13), with resistivity included, in the form

$$\left(\frac{\partial}{\partial t} + \mathbf{u}_i \cdot \nabla - \lambda_\Omega \nabla^2\right) B = -B \nabla \cdot \mathbf{u}_i. \qquad (25)$$

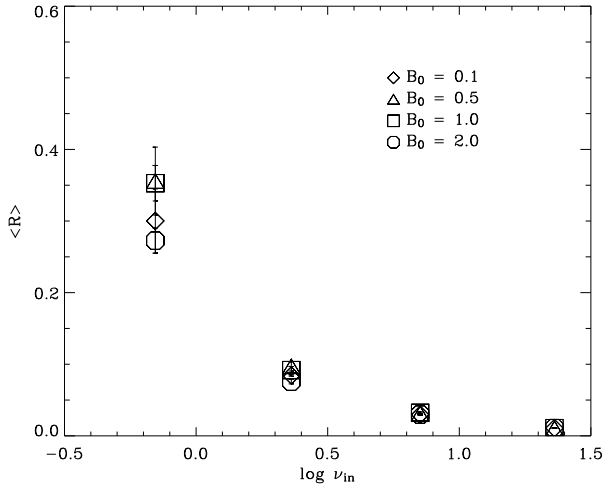

FIG. 13.— Mean ratio of rms divergence over rms curl of $\mathbf{u}_i$, $R = |\nabla \cdot \mathbf{u}_i|/|\nabla \times \mathbf{u}_i|$ against ν_{in} for background field strengths B_0 as denoted in the plot. Error bars denote the standard deviation about the mean. Means were taken over the full computational domain.

The second term on the LHS of equation (25) represents advection. It is predominantly, although not entirely, advection by the GP flow. As such, it cascades power to $n\kappa_f \pm 1$, just as occurs for the tracer. The RHS of equation (25) represents compression. Here the GP flow plays no role. If the inhomogeneous part of B were less than the mean part, the RHS could be approximated by $B_0 \nabla \cdot \mathbf{u}_i$ and the Fourier spectrum of $\nabla \cdot \mathbf{u}_i$ would map directly to that of B. Since B is roughly twice B_0, this is only part of the story; the compression term gives significant nonlinear coupling. In any case, it is clear that we must investigate the ion flow.

5.4. *The Ion Flow*

The ion flow is driven by friction with the neutrals, by magnetic pressure, and by its own Reynolds stress. Friction drives $\mathbf{u}_i$ toward $\mathbf{u}_{GP}$. The Reynolds stress is nonlinear, and drives compressive flow at multiples of κ_f. The magnetic field begins with power in the $(1, 1)$ and $(0, 0)$ components. This power is cascaded to smaller scales by advection, but is also coupled to the compressive part of the ion flow. The Lorentz force itself is nonlinear, creating additional harmonics in the ion flow.

We measure the compressibility of the flow through the parameter $\langle R \rangle$, the ratio of the rms divergence of $\mathbf{u}_i$ to its rms curl. Figure 13 shows $\langle R \rangle$ as a function of ν_{in} for four magnetic fieldstrengths. At the lowest collision frequency the divergence is a few tenths the curl, but quickly decreases with increasing ν_{in}. The value of B influences $\langle R \rangle$ less than the value of ν_{in} does, and $\langle R \rangle$ is not monotonic in B. At low B, Lorentz forces are insignificant and compression arises from the Reynolds stress. As B increases, Lorentz forces begin to play a role and lead to some additional compression. As B increases further, the field resists compression and actually reduces $\nabla \cdot \mathbf{u}_i$.

The spectra of the u_{ix} and $\nabla \cdot \mathbf{u}_i$ are shown in Figures 14 and 15 . There is substantial power in both quantities at κ_f and its multiples. This can be attributed

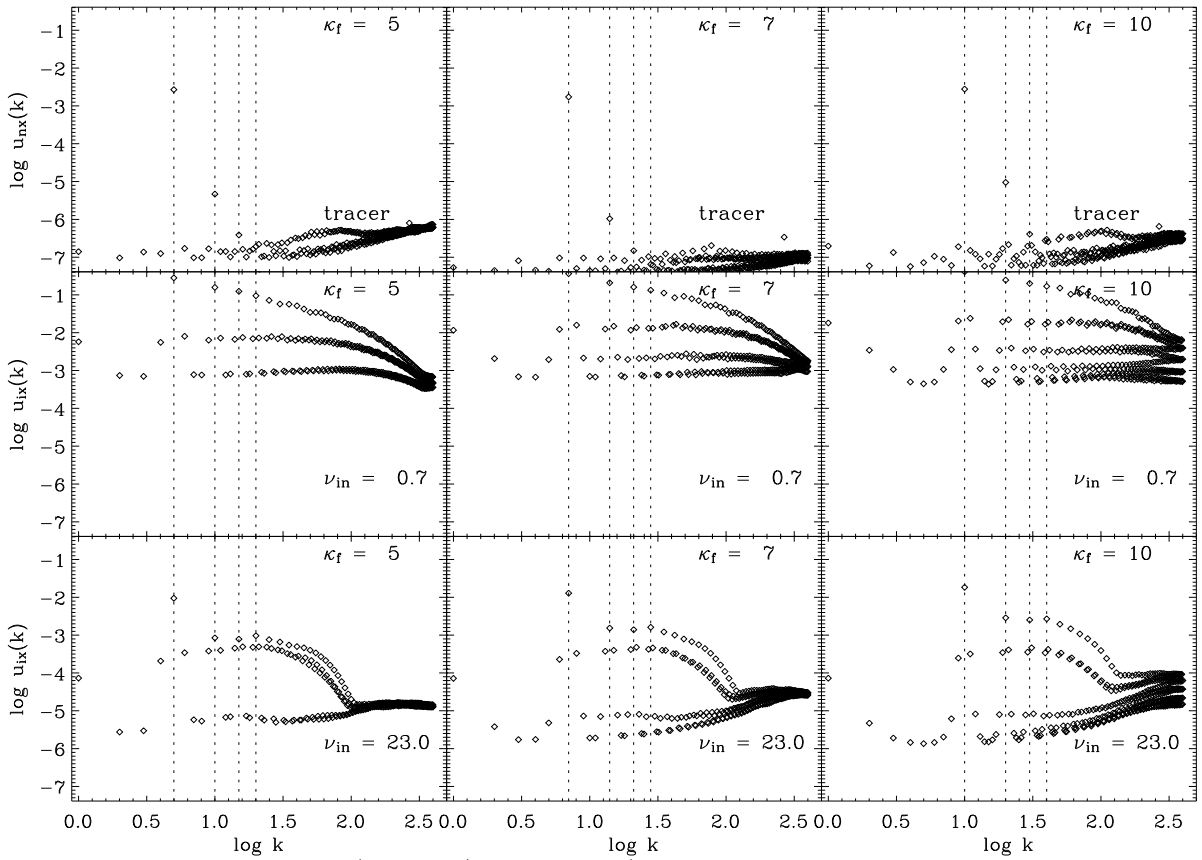

FIG. 14.— Fourier spectra of u_{nx} (upper row) and and u_{ix} (lower rows for minimum and maximum collision frequency ν_{in}) for $\kappa_f \in \{5, 7, 10\}$. Vertical dashed lines denote multiples of κ_f (see text). Resolution $N = 801^2$.

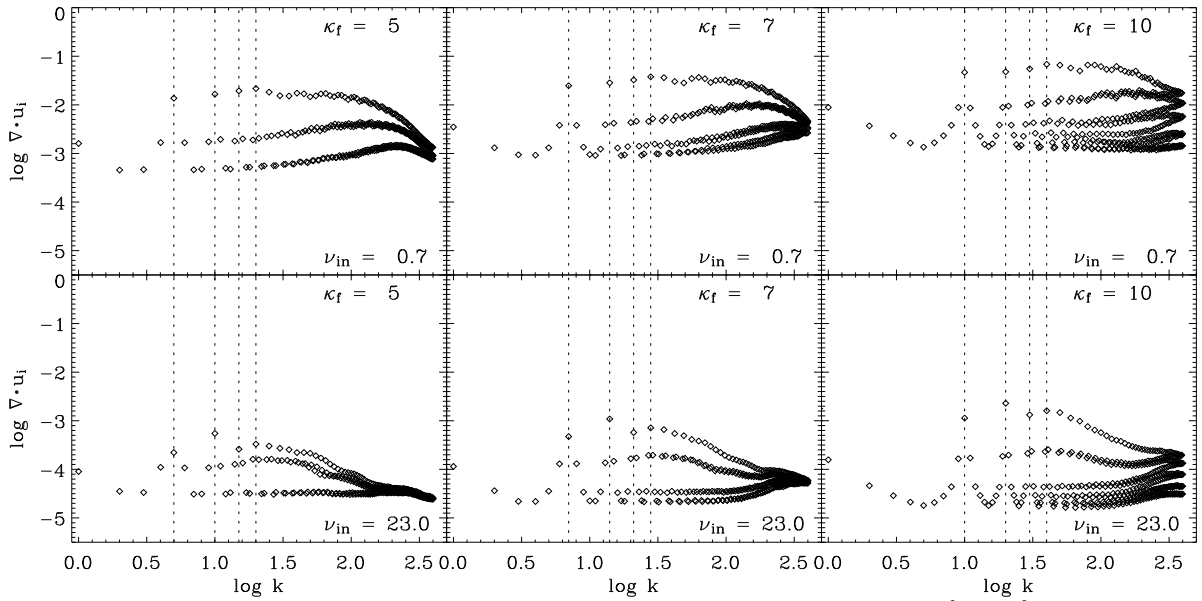

FIG. 15.— Fourier spectra of $\nabla \cdot \mathbf{u}_i$ for minimum and maximum collision frequency ν_{in} and $\kappa_f \in \{5, 7, 10\}$. Vertical dashed lines denote multiples of κ_f. Resolution $N = 801^2$. By definition, $\nabla \cdot \mathbf{u}_n \equiv 0$.

primarily to frictional driving by $\mathbf{u}_{GP}$ with generation of power at the multiples of κ_f by $\mathbf{u}_i \cdot \nabla \mathbf{u}_i$. The peak in the spectrum of u_{ix} at κ_f reflects the close correspondence between the ion flow and the GP flow. The spectrum of $\nabla \cdot \mathbf{u}_i$, however, is peaked not at κ_f, but at its second or fourth multiple. The lower the collisionality, the higher the peak. The flow generated by the nonlinear Reynolds stress as the GP flow beats together with itself is compressive, and these flows themselves generate higher harmonics yet. If there were no Lorentz force, the spectrum of $\mathbf{u}_i$ would consist purely of harmonics of the GP flow. The magnetic field, however, is cascaded by nonlinear

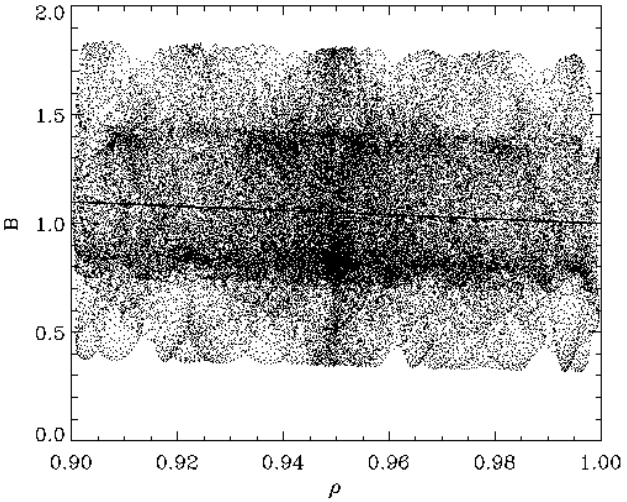

FIG. 16.— Magnetic field strength B against density ρ after one eddy turnover time τ_f for $k_f = 5$ and $\nu_{in} = 0.7$. The line denotes the initial condition, and simultaneously the result when B is subjected to turbulent diffusion only, but not AD, after one τ_f.

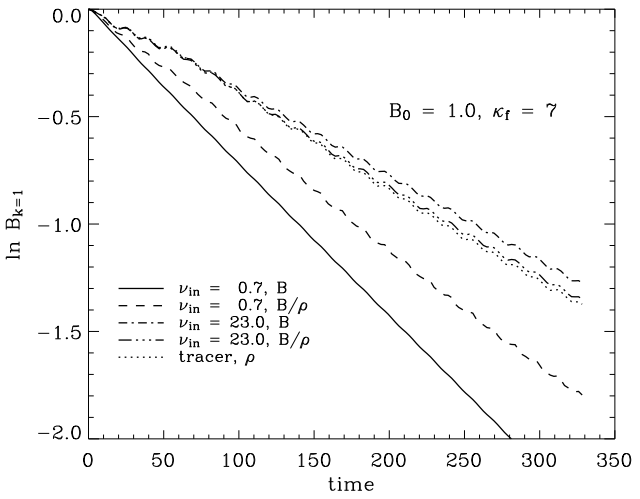

FIG. 17.— Decay of the $(k = 1)$-component of B and B/ρ against time for $\nu_{in} \in \{0.7, 2.3\}$.

advection to the sideband wavenumbers $n\kappa_f \pm 1$. The resulting power in the magnetic pressure gradient fills in the spectrum of $\mathbf{u}_i$ at other wavenumbers.

In the interstellar medium, the respective magnitudes of the Reynolds stress and Lorentz force terms may well be reversed. As we commented below equation (22), numerical considerations compel us to make v_f/c_{Ai} unrealistically large. However, both these terms are nonlinear, and both cascade the ion flow to small scales.

5.5. *Diffusion of B/ρ*

Finally, we turn to the $B - \rho$ relation itself. A direct demonstration of how quickly B/ρ changes for the GP-flow in combination with AD is given in Figure 16. After one eddy turnover time, the initially strict correlation between B and ρ (solid line) is completely destroyed. The solid line also represents the correlation $B(\rho)$ for B subject to the GP-flow alone, not including AD. In that case, B and ρ are both tracer fields, and diffuse in the same manner.

The separation of B and ρ on small scales is reflected in the decay of the largescale, or $(\pm 1, \pm 1)$ component of B/ρ (Fig. 17). Since – neglecting numerical diffusion – ρ ranges only from 0.9 to 1.1, we have to a fairly good approximation

$$\left(\frac{B}{\rho}\right)_{k=1} \approx \frac{B_{k=1}}{\rho_0} - \frac{B_0}{\rho_0}\frac{\rho_{k=1}}{\rho_0}. \qquad (26)$$

Since both $B_{k=1}$ and $\rho_{k=1}$ decay (see Fig. 17), it is clear that $(B/\rho)_{k=1}$ must decay as well, at least in the limit represented by equation (26). The decay rate estimated by equation (26) approximates the actual decay rate quite well.

6. SUMMARY

The magnetic fieldstrength - density relation in the interstellar medium is observed to be quite weak, particularly in the atomic component and through the transition from diffuse gas to GMCs. The flatness of the trend is consistent with field-aligned flow or with an enhanced diffusion rate. This paper is concerned with testing the hypothesis that the diffusion rate is due to ambipolar drift accelerated by turbulence. We report on a series of numerical experiments intended to complement, and in some ways extend, analytical work on this problem by Fatuzzo & Adams (2002), Kim & Diamond (2002), and Zweibel (2002). Within the framework of interstellar medium physics, the setup is best imagined as small scale turbulence acting on a relatively well ordered field.

We assumed a 2.5D geometry in which the motions are perpendicular to the magnetic field $\hat{\mathbf{z}}B$ and independent of z. In this situation, the fieldlines are shuffled but not bent, and there is no magnetic tension force. This type of turbulence is expected in a strong magnetic field (Strauss 1976) or as the outcome of an MHD cascade (Goldreich & Sridhar 1995), although in completely suppressing variation with z we have taken this description to an extreme degree.

We imposed a flow of the type considered by Galloway & Proctor (1992) (see eq. [18]) on the neutrals. The GP flow is spatially and temporally periodic, divergence free, and chaotic. This flow lacks some obvious features of interstellar turbulence, notably compressibility and a full spectrum of spatial scales. We chose this flow because it can be written in closed form, its level of chaos can be tuned by specification of a single parameter, and it is known to produce eddy diffusion. This made it a good candidate for a first series of numerical experiments. The basic assumption that the neutral flow can be prescribed as independent of Lorentz forces can be justified in either one of two ways. If the magnetic field were well below equipartition with the turbulent flow, this assumption would be valid independent of scale. This is, however, generally not the situation in the interstellar medium. Alternatively, we could restrict the computation to eddy sizes less than the cutoff wavenumber for strongly coupled MHD wave propagation; $k > 2(\rho_i/\rho_n)^{1/2}\nu_{in}/c_{Ai}$ We emphasize, however, that this restriction is only a self consistency requirement for our calculation, not for

turbulent ambipolar diffusion itself.

We assumed a weakly ionized gas in which the bulk density ρ is advected with the flow equal to the GP flow and the ion density ρ_i is kept constant (see §3 3.5). We solved the ion momentum equation (eq. [12]) including the full nonlinear advection operator, the magnetic pressure gradient, and friction with the neutrals. This allowed us to go beyond the strong coupling approximation (eq. [5]) made in the analytical work. However, we chose the GP wavenumber κ_f low enough that there would still be substantial friction in an eddy turnover time (eq. [22]). The magnetic field is advected and compressed by the ion flow, and subject to a small amount of resistive diffusion, according to equation (13).

Our primary consideration, in choosing the computational scheme, was to minimize the role of numerical diffusion. Tests of the code based on linear theory, on measured rates of laminar diffusion, and with regards to resolution are shown in Figures 1, 8 and 11. By scrupulous choice of parameter regime we are able to keep the anomalous growth of small scale structure to a few percent or less while still considering collision frequencies varying by a factor of slightly more than 30, magnetic fieldstrengths over a factor of 20, and up to a factor of 10 between the large scale quantities to be diffused and the GP eddies.

The most serious physical shortcomings of the model, as a realization of interstellar turbulence, are its restricted geometry, kinematic prescription for the neutral flow, and relatively large ratio of turbulent speed to ion Alfvén speed. Although all three of these features were to some extent forced upon us by numerical considerations, we see some advantages to the first two, which have enabled us to study turbulent ambipolar diffusion in a relatively uncomplicated setting without a bevy of competing physical effects. The main consequence of the third feature is that it makes the Reynolds stress overly prominent in comparison to the Lorentz stress. However, even when $\nabla \cdot \mathbf{u}_i$ is relatively small, the differences between $\mathbf{u}_i$ and $\mathbf{u}_{GP}$ are significant enough on small scales to decorrelate B and ρ (Fig. 13).

These are the main results of our calculations:

1. The GP flow causes decay of the large scale component of the density (or any other tracer field). The decay is brought about by mixing to small scales. Despite the relatively small number of eddies in the system, the decay rate is well described by a turbulent diffusivity of order v_f/k_f, as expected from mixing length theory. The decay of the tracer is shown in Figure 8.

2. The ion flow driven by the GP flow causes decay of the largescale component of B. At the largest value of ν_{in} in our experiment, the decay rate is close to the decay rate of the tracer. At the smallest value, it is faster. We attribute this, at least in part, to the substantial role of laminar diffusion in this case. The eddy diffusivity is nearly independent of the microscopic diffusivities (Ohmic and ambipolar), and of the numerical resolution. The decay of the field is shown in Figure 8.

3. Although the large scale structure in ρ and B decay at similar rates, the large scale structure in their ratio, B/ρ, decays at the eddy rate as well, as shown in Figure 17. This is brought about by the differences between $\mathbf{u}_{GP}$ and $\mathbf{u}_i$ on small scales. These small scale relative drifts rapidly destroy any correlation between B and ρ, as shown in Figure 16. Thus, neither point to point measurements nor line of sight averages would yield a $B-\rho$ relation. We regard the separate transport of B and ρ as Eulerian transport, and the decay of B/ρ as Lagrangian transport.

What are the implications for the interstellar medium? The enhanced diffusion rate demonstrated here must be balanced against large scale compressive flows, which act to restore the $B-\rho$ relation. There is evidence that in environments such as H I shells, which are produced by strong dynamical compression and which show relatively strong magnetic fields, turbulence is secondary to flow. This may also be the case in dense molecular gas, in which frictional damping of the turbulence is too strong to permit the small scale ion-neutral drifts necessary for diffusion. In future work, we intend to include full neutral dynamics, which would allow such flows, driven, for example, by cooling, or by self gravity. This would also allow an improved realization of the turbulent spectrum. Inclusion of a third dimension would permit us to examine the role of field aligned flow, and to consider stretching as well as compression of the field. Both can affect the $B-\rho$ relation.

Finally, we mention some other applications of turbulent diffusion of the magnetic field with respect to the gas. It may play an important role in the escape of the large scale horizontal field from the Galactic disk. It may also permit the mixing of stellar fields with *in situ* fields in weakly ionized accretion disks, and jet fields with ambient fields in outflows from young stars.

We thank N. C. Brummell for enlightening discussions. F. H. is grateful for support by a Feodor-Lynen fellowship of the Alexander-von-Humboldt Foundation. A. S. acknowledges the support of a Fellowship from the UK Astrophysical Fluids Facility (UKAFF). The research of J. E. G. D. at Oxford is funded by the Leverhulme Trust. S. Jansen built the local PC cluster, which was used, together with the SGI Origin 2000 machines of the National Center for Supercomputing Applications at the University of Illinois, for the computations in this paper. This work was supported by NSF grants AST-0098701 and AST-0328821, and the Graduate School of the University of Wisconsin, Madison. The Center for Magnetic Self-Organization in Laboratory & Astrophysical Plasmas is funded by the National Science Foundation. A minor issue of phrasing was settled with the help of the U.S. Mint.

APPENDIX

MEASUREMENT OF TURBULENT DIFFUSION

Most discussions of turbulent diffusion are based on quasilinear theory. We provide a brief review of quasilinear diffusion theory here; for details and a more rigorous derivation see e.g. Moffatt (1978).

Consider a quantity q which evolves according to the advection - diffusion equation

$$\left(\frac{\partial}{\partial t} + \mathbf{u}\cdot\nabla\right) q = \nabla\cdot\lambda\nabla q \tag{A1}$$

where λ is the microscopic diffusivity. Assume q can be decomposed into a mean part $\langle q\rangle$, the ensemble average of q, and a fluctuating part δq with zero mean, while $\mathbf{u}$ has zero mean and is isotropic. Averaging equation (A1) gives

$$\frac{\partial\langle q\rangle}{\partial t} = -\langle\mathbf{u}\cdot\nabla\delta q\rangle + \nabla\cdot\lambda\nabla\langle q\rangle. \tag{A2}$$

We solve for δq by subtracting equation (A2) from equation (A1) and discarding the terms quadratic in the fluctuations. The result is

$$\frac{\partial\delta q}{\partial t} = -\mathbf{u}\cdot\nabla\langle q\rangle + \nabla\cdot\lambda\nabla\delta q. \tag{A3}$$

If the correlation time τ of the turbulence is short compared to the diffusion time, the solution of equation (A3) is approximately

$$\delta q \sim -\int^t \mathbf{u}\cdot\nabla\langle q\rangle dt'. \tag{A4}$$

Substituting equation (A4) into equation (A2) and averaging over an ensemble gives

$$\frac{\partial\langle q\rangle}{\partial t} = \nabla\cdot\left(\lambda_e + \lambda\right)\nabla\langle q\rangle, \tag{A5}$$

where

$$\lambda_e \sim u^2\tau \tag{A6}$$

is the turbulent diffusivity.

Equation (A2) shows that turbulent transport is the result of the turbulent velocity field $\mathbf{u}$ beating together with fluctuations in the field to be transported, in this case q. With the assumption that the scales of the mean and fluctuating fields are well separated, δq is proportional to the local gradient of $\langle q\rangle$, and the turbulent flux has the same form as a diffusive flux. An immediate implication of equation (A2) is that if $\langle q\rangle$ is initially a Fourier mode; $\langle q\rangle(\mathbf{x},0) = \langle\tilde{q}\rangle\exp\left(i\mathbf{k}\cdot\mathbf{x}\right)$, then $\langle q\rangle$ decays exponentially, with

$$\langle q\rangle(\mathbf{x},t) = \langle\tilde{q}\rangle\exp\left(-\lambda_e k^2 t + i\mathbf{k}\cdot\mathbf{x}\right). \tag{A7}$$

In order to investigate whether large scale quantities undergo turbulent diffusion in our simulations, we integrate equation (A5) over a domain of area A with boundary contour C. Using Gauss's theorem we derive

$$\frac{\partial}{\partial t}\int_A \langle q_{k=1}\rangle dxdy = \left(\lambda_e + \lambda\right)\int_C \mathbf{n}\cdot\nabla\langle q_{k=1}\rangle dl, \tag{A8}$$

where we assume λ_e and λ are spatially constant. The total diffusion coefficient D is the ratio of the left hand side of equation (A8) to the right hand side.

We isolate the large scale fields in our model by setting all modes in the Fourier transform to zero, except the ones corresponding to $k_{x,y} = \pm 1$. We label the resulting quantity $q_{k=1}$. We identify the average of $q_{k=1}$ over one GP flow period τ_f, $\langle q_{k=1}\rangle$, with $\langle q\rangle$. Since the domain average of $\langle q\rangle$ is zero, we choose A to cover one quarter of the computational domain, centered on the maximum of the initial magentic field perturbation. Computing the left and right hand sides of equation (A8) leads to an expression for D

$$D = \frac{\partial}{\partial t}\int_A \langle q_{k=1}\rangle dxdy \Big/ \int_C \mathbf{n}\cdot\nabla\langle q_{k=1}\rangle dl. \tag{A9}$$

REFERENCES

Bourke, T. L., Myers, P. C., Robinson, G., & Hyland, A. R. 2001, ApJ, 554, 916

Brandenburg, A. & Zweibel, E. G. 1995, ApJ, 448, 734

Brummell, N. H., Cattaneo, F., Tobias, S. M. 2001, *Fl. Dyn. Res.*, 28, 237

Crutcher, R. M. 1999, ApJ, 520, 706

Drazin, P. G. 1992, *Nonlinear Systems*, pp 140 - 143 (Cambridge: Cambridge University Press)

Fatuzzo, M. & Adams, F. C. 2002, ApJ, 570, 210

Galloway, D. J. & Proctor, M. R. E. 1992, Nature, 356, 691

Goldreich, P.M. & Sridhar, S. 1995, ApJ, 438, 763

Heitsch, F. & Zweibel, E. G. 2003, ApJ, 583, 229

Kim, E.-J. & Diamond, P. H. 2002, ApJ, 578, 113

Kulsrud, R. & Pearce, W. P. 1969, ApJ, 156, 445

Mac Low, M.-M, Norman, M. L., Königl, A. & Wardle, M. 1995, ApJ, 442, 726

Mac Low, M.-M & Smith, M. D. 1997, ApJ, 491, 596
Mestel, L. 1985, in Protostars and Planets II, ed. D. C. Black & M. S. Matthews (Tucson: Univ. Arizona Press), 320
Moffatt, H.K. 1978, in *Magnetic field generation in electrically conducting fluids*, Cambridge Univ. Press, Cambridge
Sarma, A.P., Troland, T.H., Crutcher, R.M. & Roberts, D.A. 2002, ApJ, 580, 928
Soward, A. M. 1994, in Lectures on Solar and Planetary Dynamos, Publications of the Newton Institute, Vol. 2., Cambridge University Press, 181
Strauss, H.R. 1976, Phys. Fluids, 19, 134
Tang, H. Z. & Xu, K. 2000, J. Comp. Phys., 165, 69
Tóth, G. 1995, MNRAS, 274, 1002
Troland, T. H. & Heiles, C. 1986, ApJ, 339, 345
Xu, K. 1999, J. Comp. Phys., 153, 334
Zweibel, E. G. 2002, ApJ, 567, 962